



HAL
open science

Imaging Topological Defects in a Noncollinear Antiferromagnet

Aurore Finco, Angela Haykal, Stéphane Fusil, Pawan Kumar, Pauline Dufour, Anne Forget, Dorothée Colson, Jean-Yves Chauleau, Michel Viret, Nicolas Jaouen, et al.

► **To cite this version:**

Aurore Finco, Angela Haykal, Stéphane Fusil, Pawan Kumar, Pauline Dufour, et al.. Imaging Topological Defects in a Noncollinear Antiferromagnet. *Physical Review Letters*, 2022, 128 (18), pp.187201. 10.1103/PhysRevLett.128.187201 . hal-03659802

HAL Id: hal-03659802

<https://hal.science/hal-03659802>

Submitted on 5 May 2022

HAL is a multi-disciplinary open access archive for the deposit and dissemination of scientific research documents, whether they are published or not. The documents may come from teaching and research institutions in France or abroad, or from public or private research centers.

L'archive ouverte pluridisciplinaire **HAL**, est destinée au dépôt et à la diffusion de documents scientifiques de niveau recherche, publiés ou non, émanant des établissements d'enseignement et de recherche français ou étrangers, des laboratoires publics ou privés.

Imaging topological defects in a non-collinear antiferromagnet

Aurore Finco,¹ Angela Haykal,¹ Stéphane Fusil,² Pawan Kumar,¹ Pauline Dufour,² Anne Forget,³ Dorothée Colson,³ Jean-Yves Chauleau,³ Michel Viret,³ Nicolas Jaouen,⁴ Vincent Garcia,² and Vincent Jacques¹

¹*Laboratoire Charles Coulomb, CNRS, Université de Montpellier, 34095 Montpellier, France*

²*Unité Mixte de Physique, CNRS, Thales, Université Paris-Saclay, 91767 Palaiseau, France*

³*SPEC, CEA, CNRS, Université Paris-Saclay, 91191 Gif sur Yvette, France*

⁴*Synchrotron SOLEIL, 91192 Gif-sur-Yvette, France*

(Dated: March 30, 2022)

We report on the formation of topological defects emerging from the cycloidal antiferromagnetic order at the surface of bulk BiFeO₃ crystals. Combining reciprocal and real-space magnetic imaging techniques, we first observe, in a single ferroelectric domain, the coexistence of antiferromagnetic domains in which the antiferromagnetic cycloid propagates along different wavevectors. We then show that the direction of these wavevectors is not strictly locked to the preferred crystallographic axes as continuous rotations bridge different wavevectors. At the junctions between the magnetic domains, we observe topological line defects identical to those found in a broad variety of lamellar physical systems with rotational symmetries. Our work establishes the presence of these magnetic objects at room temperature in the multiferroic antiferromagnet BiFeO₃, offering new possibilities for their use in spintronics.

When symmetry-breaking phase transitions occur, they induce the formation of topological defects [1], which are isolated regions of lower dimensionality corresponding to a singularity of the order parameter [2]. From topology and symmetry considerations, these defects can be identified and classified in various physical systems, from cosmological to nanometric length scales. In lamellar structures with rotational symmetries, such singular lines appear as dislocations and disclinations which have been extensively studied [3], even before the topological approach to their description was proposed. Illustrating the universality of these patterns [4], similar defects are found in a broad variety of modulated physical systems including cholesteric liquid crystals [5], ferromagnetic garnets [6] or copolymers [7]. Recently, they were also identified in the helical state of the ferromagnetic B20 material FeGe [8], providing – besides skyrmions [9] – additional topological magnetic textures for future use in spintronics.

In this work, we demonstrate that these topological defects are present in another type of chiral magnetic material, the multiferroic BiFeO₃, which displays a lamellar pattern originating from an antiferromagnetic cycloid [10] rather than a ferromagnetic helix. We start with a detailed depiction of the magnetic texture of bulk BiFeO₃, and we discuss the origin of the stray field allowing us to achieve real-space imaging of the antiferromagnetic state with scanning-NV magnetometry. Then, we use this technique to show the coexistence of three magnetic rotational domains within a single ferroelectric domain. At the junctions between these areas where the cycloids propagate along different directions, we observe either a smooth rotation of the wavevector or the formation of topological defects.

At room temperature, bulk BiFeO₃ exhibits a slightly distorted rhombohedral structure, commonly described by the pseudo-cubic unit cell shown in Fig. 1(a) [11, 12]. The Bi³⁺ ions are displaced with respect to the FeO₆

octahedra, giving rise to a large spontaneous ferroelectric polarization \mathbf{P} pointing along one of the (111) directions of the pseudo-cubic cell [13, 14]. Besides this ferroelectric behavior, BiFeO₃ is also a G-type antiferromagnet, in which the slight shift of the Fe³⁺ ions away from the center of the FeO₆ octahedra induces a magnetoelectric interaction. This interaction stabilizes an incommensurate cycloidal rotation of the Fe³⁺ magnetic moments [15], propagating along a direction \mathbf{k} perpendicular to \mathbf{P} . In bulk BiFeO₃, the period λ_b of the antiferromagnetic cycloid is around 64 nm [10, 16]. For a given polarization direction, the rhombohedral symmetry allows three equivalent cycloid propagation directions, forming three rotational magnetic domains [17]. If \mathbf{P} is along the [111] axis, the propagation vectors \mathbf{k}_1 , \mathbf{k}_2 and \mathbf{k}_3 lie in a (111) plane and point along the $[-110]$, $[0-11]$ or $[10-1]$ directions [Fig. 1(a)]. This *type I* cycloid [18–21] is the one commonly observed in bulk BiFeO₃ [10, 16, 17].

The rotation angle induced by the magnetoelectric coupling is constant from one Fe site to another along \mathbf{k} [15]. Each magnetic moment is thus compensated by its antiparallel neighbors, a fact commonly overlooked in many previous descriptions of the cycloid [16, 22]. On a scale larger than the inter-atomic distance, such an antiferromagnetic cycloid is therefore perfectly compensated, and does not produce any static magnetic fields above (001) surfaces. To explain the origin of the stray field measured above BiFeO₃ thin films [20, 23, 24], an additional Dzyaloshinskii-Moriya (DM) interaction stemming from the antiphase rotation of the oxygen octahedra [17] is required. This interaction cants the spins out of the cycloidal plane, leading to an uncompensated periodic magnetic moment \mathbf{m}_{DM} locked to the cycloid, as sketched in Fig. 1(b). The resulting spin density wave (SDW) generates a stray magnetic field whose spatial distribution depends on the cycloid wavevector. In this work, we employ scanning-NV magnetometry to image this magnetic field distribution in real space with nanoscale spatial res-

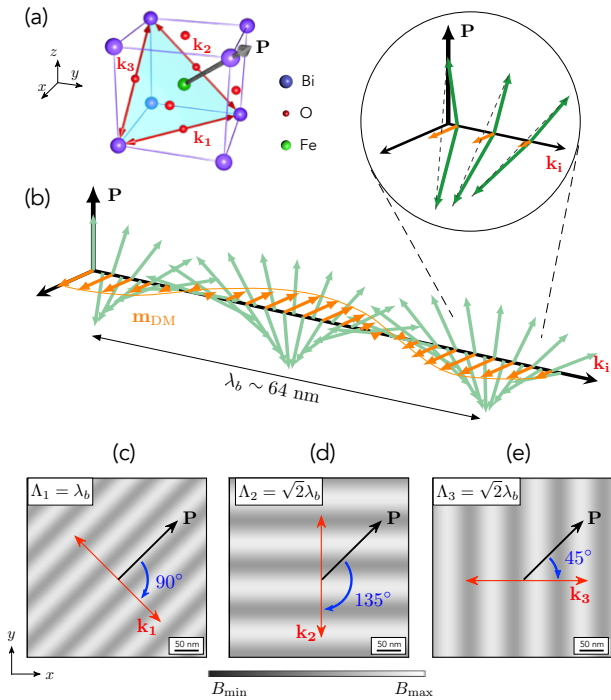


FIG. 1. (a) Sketch of the pseudo-cubic cell of BiFeO_3 showing the three possible propagation directions of the antiferromagnetic cycloid for a given ferroelectric variant. Here \mathbf{P} is pointing along the $[111]$ axis, so that $\mathbf{k}_1 \parallel [-110]$, $\mathbf{k}_2 \parallel [0-11]$ and $\mathbf{k}_3 \parallel [10-1]$. (b) Schematic representation of the cycloid propagating with a wavevector \mathbf{k}_i perpendicular to \mathbf{P} . The zoom illustrates the canting of the spins out of the cycloidal plane, leading to a spin density wave (SDW) characterized by the modulated uncompensated moment \mathbf{m}_{DM} . (c-e) Expected magnetic field maps produced by the SDW above a (001)-oriented BiFeO_3 sample, showing a modulated field amplitude whose direction and period is tied to the cycloid wavevector.

olution.

To discriminate between the possible propagation directions of the cycloid within a single ferroelectric domain, we examine their projections on the sample surface. Considering a (001)-oriented BiFeO_3 crystal, the \mathbf{k}_1 propagation vector lies in the surface plane, making an angle of 90° with the projected polarization [see Fig. 1(c)]. The corresponding SDW produces a stray field modulated along \mathbf{k}_1 with a period $\Lambda_1 = \lambda_b \sim 64 \text{ nm}$. On the other hand, the \mathbf{k}_2 and \mathbf{k}_3 propagation vectors lie out of the surface plane, with an in-plane projection angles of 135° and 45° with the in-plane polarization [Fig. 1(d,e)]. In both cases, the stray field modulation period corresponds to the projection of the intrinsic cycloid wavelength on the (001) surface plane, leading to $\Lambda_2 = \Lambda_3 = \sqrt{2} \lambda_b \sim 90 \text{ nm}$. The period and the orientation of the magnetic field pattern can therefore be used to identify the cycloid propagation vector.

Below, we investigate the antiferromagnetic order in a millimeter-sized (001)-oriented bulk BiFeO_3 crystal grown by the $\text{Bi}_2\text{O}_3\text{-Fe}_2\text{O}_3$ flux method [14]. The local

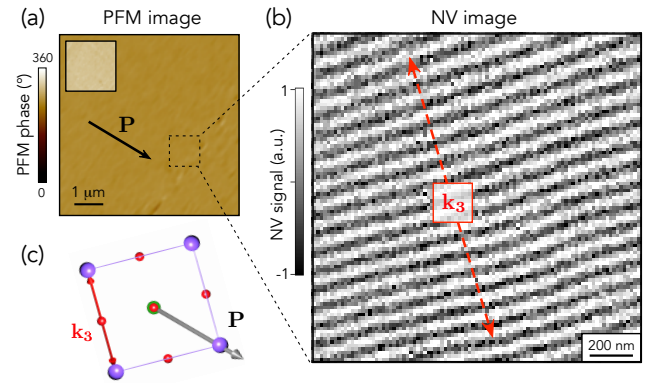


FIG. 2. (a) Out-of-plane PFM phase image recorded above the (001)-oriented bulk BiFeO_3 crystal. Inset: corresponding in-plane PFM phase image. The black arrow indicates the projection of the ferroelectric polarization \mathbf{P} on the (001) sample surface. (b) Magnetic field image recorded with the scanning-NV magnetometer operating in dual-iso-B imaging mode. The red dashed line indicates the propagation direction of the cycloid along \mathbf{k}_3 . The period of the modulation is $\Lambda_3 = 92 \pm 2 \text{ nm}$.

ferroelectric properties were first characterized through piezoresponse force microscopy (PFM). As shown in Fig. 2(a), the BiFeO_3 crystal exhibits a single ferroelectric domain, a feature that is commonly observed for bulk crystals grown by the flux method at temperatures much lower than the ferroelectric Curie temperature ($T_C \sim 1100 \text{ K}$) [16]. Combining in-plane and out-of-plane PFM measurements, the direction of the ferroelectric polarization \mathbf{P} was unambiguously identified [see black arrow in Fig. 2(a)]. The corresponding antiferromagnetic texture was imaged with a scanning-NV magnetometer operating under ambient conditions (see [25] and Supplemental Material [26]). We use the magnetometer in dual-iso-B imaging mode to characterize the magnetic field distribution produced by the SDW bounded to the cycloid. A typical image recorded above a single ferroelectric domain is shown in Fig. 2(b). Here the magnetometer signal is modulated along a direction making an angle of about 45° with the in-plane component of \mathbf{P} . This observation indicates an out-of-plane propagation of the cycloid along \mathbf{k}_3 [Fig. 2(c)], which is further supported by the measured period of the modulation $\Lambda_3 = 90 \pm 2 \text{ nm}$. In this micron-sized area of the sample, we thus observe a single rotational magnetic domain. This experiment constitutes the first real-space observation of the non-collinear antiferromagnetic order in a bulk BiFeO_3 crystal. To estimate the uncompensated magnetic moment m_{DM} of the SDW, a quantitative magnetic field image was recorded [25] and fitted using the analytical expression of the stray field produced by the magnetic texture [22]. This analysis leads to $m_{\text{DM}} = 0.09 \pm 0.03 \mu_B$ (see Supplemental Material [26]), in good agreement with the value inferred through polarized neutron scattering experiments [17].

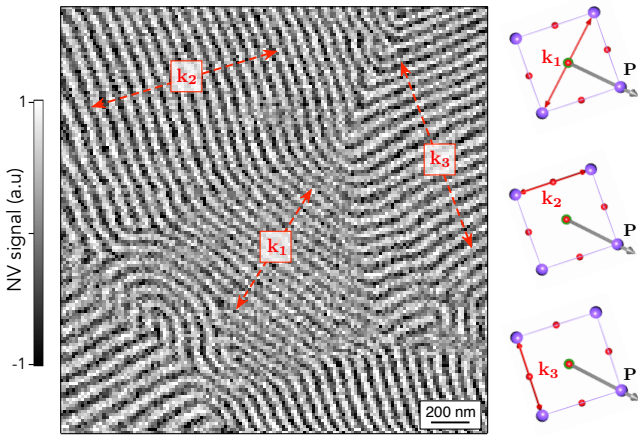


FIG. 3. NV magnetometry image recorded in dual-iso-B mode showing the coexistence of the three propagation directions of the cycloid (red dashed arrows) in a single ferroelectric domain of the bulk BiFeO₃ crystal.

With this set of results, it is tempting to conclude that the antiferromagnetic order in our BiFeO₃ crystal consists in a single cycloid variant, as reported previously using neutron scattering [16]. However, magnetic measurements performed on different regions of the crystal reveal more complex configurations. As an example, Figure 3 shows another magnetic image in which the three different cycloid propagation directions are simultaneously observed within a single ferroelectric domain. Each cycloid variant was identified from the orientation of the magnetic field modulation with respect to the in-plane component of \mathbf{P} [Fig. 1(c-e)]. In addition, the modulation period was measured along line profiles in each magnetic domain, leading to $\Lambda_1 = 59 \pm 2$ nm, $\Lambda_2 = 82 \pm 2$ nm, and $\Lambda_3 = 94 \pm 2$ nm. These values are in fair agreement with the expected projections of the cycloid wavevectors on the (001) surface plane. Such a multi- \mathbf{k} domain structure is in stark contrast with the magnetic order observed in BiFeO₃ thin films, in which a magnetic anisotropy resulting from epitaxial strain lifts the degeneracy between the three possible wavevectors, stabilizing a single cycloid variant [18, 20].

Earlier high-resolution neutron diffraction experiments performed on bulk BiFeO₃ crystals have also revealed the coexistence of the three cycloid variants, with a predominance of \mathbf{k}_1 domains [17, 27]. However, we note that for single crystals from the same batch as the ones used in this work, a single propagation direction along \mathbf{k}_1 was detected by neutron diffraction [16]. Thus, the nucleation and growth of a single spin cycloid among the three possible ones seems to be favored in the crystal core, and split into a more complex multi- \mathbf{k} domain structure at the surface. Indeed, while neutron diffraction probes the full sample volume, scanning-NV magnetometry is only sensitive to stray fields generated by the last 30-50 nm of the crystal from its surface. To reconcile bulk and surface observations, we can assume that surface symme-

try breaking is associated to a depolarizing electric field, which might perturb the cycloidal ordering through the magnetoelectric coupling. Indeed a not fully screened polarization would produce an extra (negative) electric field component along [001]. Because the magnetoelectric effect favors cycloids with magnetic moments contained in their (\mathbf{E}, \mathbf{k}) plane and wavevectors perpendicular to the total electric field, our (001) surface would weaken the \mathbf{k}_1 cycloidal state compared to \mathbf{k}_2 and \mathbf{k}_3 (affected equally). Therefore, a bulk \mathbf{k}_1 cycloid would be destabilized at the surface and could thus produce the multi- \mathbf{k} domain structure observed here. In addition, there are reports pointing to the existence of a 5 nm thick charge-depleted surface layer different from the bulk in some BiFeO₃ single crystals [28, 29]. It is not clear whether such a skin layer exists in our crystals as (i) magnetic structures do reach the surface as demonstrated by the reported exchange bias properties [30] and (ii) a weakening of polarization would imply a longer cycloidal period not observed in our measurements. It is also unclear how such a skin layer might influence the stabilization of the multi- \mathbf{k} state. Further theoretical inputs are highly desirable to explore this issue.

The magnetic image shown in Figure 3 indicates that the transition between the magnetic domains is realized either via a smooth wavevector rotation or through the formation of complex whirling structures. This is further illustrated by Figure 4(a) showing another region of the crystal, in which the cycloid propagation direction is continuously rotating such that the boundaries of magnetic domains can hardly be identified. The Fourier transform of this image features an elliptic shape, illustrating that the continuous rotation of the cycloid wavevector is correlated with a variation of the magnetic modulation period [Fig. 4(b)]. The major axis of the ellipse corresponds to the in-plane propagation direction \mathbf{k}_1 , while the two diffused satellites centered at $\pm 45^\circ$ from this axis are associated to \mathbf{k}_2 and \mathbf{k}_3 . We note that the spots corresponding to \mathbf{k}_1 are less intense because of the dominance of the out-of-plane variants in this specific image.

To get a larger scale insight on this cycloid propagation rotation, we measured the wavevector's norm and orientation with respect to \mathbf{P} in different regions of the sample. The results are gathered in the polar diagram shown in Figure 4(c). The plotted ellipse (red solid line) is the projection onto the surface plane of a circle with radius $2\pi/\lambda_b$ in the (111) plane (see Fig. 1(a) and Supplemental Material [26]). All experimental data points fall along this ellipse, with a dispersion reflecting the large spread of cycloid propagation directions. This rotation of the cycloid wavevector in the (111) plane results from the connection between the different rotational magnetic domains. Complementary measurements were performed in reciprocal space using resonant elastic X-ray scattering (REXS) at the Fe L -edge [31, 32], allowing a large surface scale to be integrated (typically of the order of 100 μm compared to 1 μm for scanning-NV magnetometry). This technique, which uses soft X-rays in reflectiv-

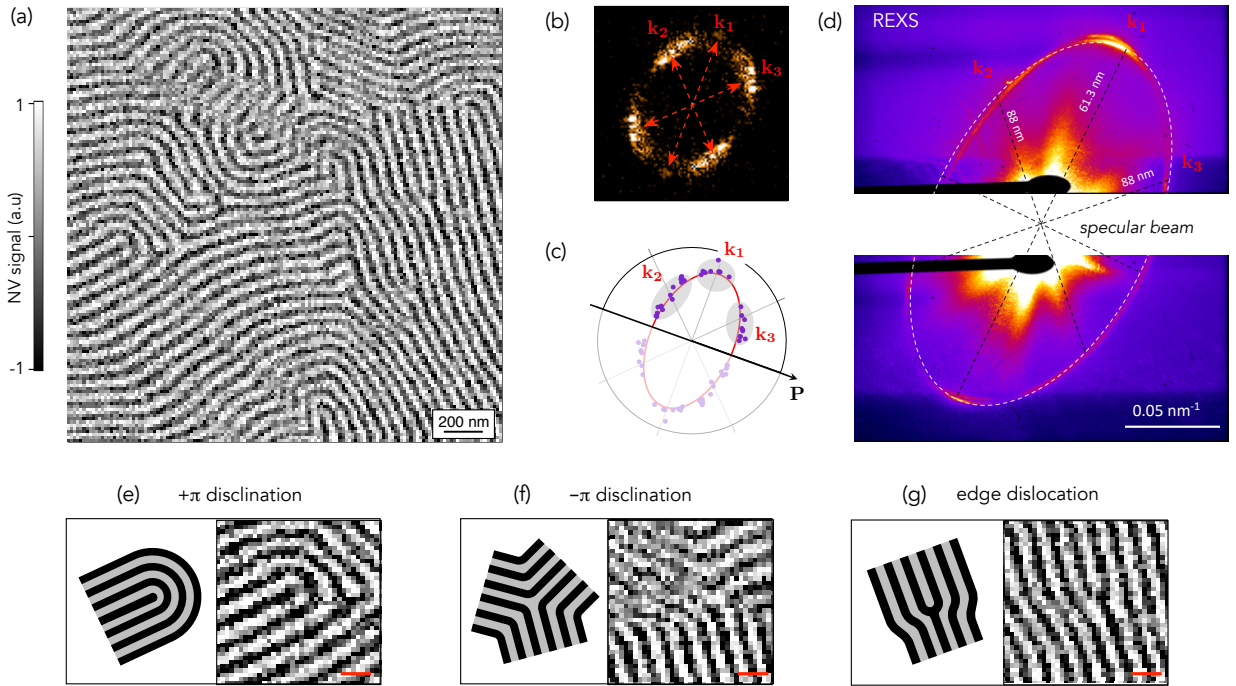


FIG. 4. (a) NV magnetometry image recorded in dual-iso-B mode showing a continuous rotation of the cycloid propagation direction. (b) Fourier transform of the magnetic image (a). The red dashed arrows indicate the three expected cycloid wavevectors. (c) Polar diagram of the in-plane projection of the wavevector obtained by measuring the period of the magnetic field modulation and its orientation with respect to \mathbf{P} in different regions of the sample. The red ellipse is the projection on the surface plane of the circle with radius $2\pi/\lambda_b$ in the (111) plane. The shaded area of the diagram is reconstructed by symmetry. (d) Resonant elastic X-ray scattering (REXS) at the Fe L -edge (708.78 eV). (e-g) Sketches and corresponding NV magnetometry close views of the different topological defects found in bulk BiFeO_3 : $\pm\pi$ -disclinations and edge dislocations. The scale bars correspond to 100 nm, the perturbation of the lamellar state induced by the defects is typically enclosed in a circle of radius $2\lambda_b$ [26].

ity geometry, mostly probes the projection of the cycloid onto the surface plane, as the typical absorption length around the Fe L -edge is only a few tens of nm from the crystal surface. Therefore, similarly to the scanning-NV measurements, it is only sensitive to the surface magnetic state. As shown in Figure 4(d), we obtain an elliptical diffraction pattern from the REXS experiment, which nicely corroborates the results obtained in real space with scanning-NV microscopy, **although the large scale averaging leads to a different distribution of the signal intensity between the \mathbf{k} -directions**. Furthermore, the ellipse long axis of 62 nm corresponds to the in-plane \mathbf{k}_1 vector while its short axis of 108 nm aligns in between the \mathbf{k}_2 and \mathbf{k}_3 vectors. This enhanced projected period at the short axis indicates that the continuous rotation of the propagation vectors could step by the $[11\bar{2}]$ crystallographic axis, identified as the *type II* cycloid. Indeed, recent experiments have shown that such an alternative cycloid can be stabilized in epitaxial BiFeO_3 thin films [18–21]. This exotic cycloidal order appears to have a period similar to the *type I* cycloid and can propagate along three possible directions: $\mathbf{k}'_1 \parallel [-211]$, $\mathbf{k}'_2 \parallel [1 - 21]$ and $\mathbf{k}'_3 \parallel [11 - 2]$, which are all contained in the (111) plane [20]. The continuous rotation of the

propagation vector between its three main components in single crystals might then be mediated by the exotic cycloid, as supported by theoretical predictions of multiple propagation vectors in BiFeO_3 [33].

Going back to the magnetic configuration presented in Fig. 4(a), we now focus on the boundaries between the rotational domains, where we expect the formation of the topological defects which are typically found in lamellar structures [4]. Fig. 4(e)-(g) display selected regions of the larger scale images shown in Figs. 3 and 4(a), where singularities can be identified. Although the lack of complete translational invariance in lamellar systems prevents a rigorous topological classification of these defects [2], the naive generalization of this approach allows us to describe such singularities, considering that the order parameter is the cycloid propagation direction. The textures presented in Figs 4(e) and (f) are $\pm\pi$ -disclinations, as the cycloid wavevector direction covers only half a circle (rotating in opposite senses for the two defects) when we follow a contour enclosing the singularity. The edge dislocation shown in Fig. 4(g) corresponds to a combination of the $+\pi$ and $-\pi$ -disclinations. Such edge dislocations have a winding number of 0 or $\pm 1/2$ depending on the distance between the two discli-

nations [8, 34]. Albeit these defects do not have a well-defined or finite integer winding number, meaning that topology does not prevent their annihilation, they are stabilized by the cycloidal lamellar structure resulting from the interplay between the different magnetic interactions in BiFeO₃. Our NV magnetometry images of the topological defects are strikingly similar to the MFM images obtained in the ferromagnet FeGe [8], even if they do not arrange along straight domain walls separating regions where the magnetic spiral propagates along different directions. As discussed previously from the large spread of the data points on the ellipse in Figs. 4(c) and (d), it appears that the cycloid wavevector in bulk BiFeO₃ is not strictly locked to the expected crystallographic directions at the vicinity of the crystal surface. This weak anisotropy allows both the smooth transitions between the rotational domains and the formation of isolated defects.

To conclude, we have studied the cycloidal antiferromagnetic order at the surface of a bulk BiFeO₃ crystal. Combining reciprocal and real-space magnetic imaging techniques, we have shown the coexistence of antiferromagnetic domains in which the cycloid propagates along different wavevectors. In addition, owing to the nanoscale spatial resolution of scanning-NV magnetometry, we observed the formation of topological defects typical for lamellar materials at the junctions

between these domains. Our work thus demonstrates that these magnetic objects, previously observed in a chiral ferromagnet [8], can be transposed in a multiferroic antiferromagnet, offering new opportunities in terms of robustness and electrical control towards their use in spintronic devices.

The data that support this work are available in Zenodo (<https://zenodo.org/record/6390870>) with the identifier 10.5281/zenodo.6390869.

ACKNOWLEDGMENTS

We thank support from the French Agence Nationale de la Recherche (ANR) through the project TATOO (ANR-21-CE09-0033-01), the European Union's Horizon 2020 research and innovation programme under grant agreement No. 964931 (TSAR) and No. 866267 (EXAFONIS), the DARPA TEE program and a public grant overseen by the ANR as part of the 'Investissement d'Avenir' programme (LABEX NanoSaclay, ref. ANR-10-LABX-0035, SPiCY). The Sesame Ile de France IM-AGeSPIN project (No. EX039175) is also acknowledged.

-
- [1] W. H. Zurek, *Physics Reports* **276**, 177 (1996).
- [2] N. D. Mermin, *Reviews of Modern Physics* **51**, 591 (1979).
- [3] P.-G. de Gennes and J. Prost, *The Physics of Liquid Crystals* (Clarendon Press, Oxford, 1993).
- [4] M. Seul and D. Andelman, *Science* **267**, 476 (1995).
- [5] Y. Bouligand, *Dislocations in solids, Chap. 23* (North-Holland Publishing Company, 1983).
- [6] M. Seul and R. Wolfe, *Physical Review A* **46**, 7519 (1992).
- [7] J. N. Murphy, K. D. Harris, and J. M. Buriak, *PLoS One* **10**, e0133088 (2015).
- [8] P. Schoenherr, J. Müller, L. Köhler, A. Rosch, N. Kanazawa, Y. Tokura, M. Garst, and D. Meier, *Nature Physics* **14**, 465 (2018).
- [9] X. Z. Yu, N. Kanazawa, Y. Onose, K. Kimoto, W. Z. Zhang, S. Ishiwata, Y. Matsui, and Y. Tokura, *Nature Materials* **10**, 106 (2011).
- [10] I. Sosnowska, T. P. Neumaier, and E. Steichele, *J. Phys. C: Solid State Phys.* **15**, 4835 (1982).
- [11] J. M. Moreau, C. Michel, R. Gerson, and W. J. James, *Journal of Physics and Chemistry of Solids* **32**, 1315 (1971).
- [12] F. Kubel and H. Schmid, *Acta Crystallographica Section B* **46**, 698 (1990).
- [13] J. Wang, J. B. Neaton, H. Zheng, V. Nagarajan, S. B. Ogale, B. Liu, D. Viehland, V. Vaithyanathan, D. G. Schlom, U. V. Waghmare, N. A. Spaldin, K. M. Rabe, M. Wuttig, and R. Ramesh, *Science* **299**, 1719 (2003).
- [14] D. Lebeugle, D. Colson, A. Forget, M. Viret, P. Bonville, J. F. Marucco, and S. Fusil, *Phys. Rev. B* **76**, 024116 (2007).
- [15] H. Katsura, N. Nagaosa, and A. V. Balatsky, *Phys. Rev. Lett.* **95**, 057205 (2005).
- [16] D. Lebeugle, D. Colson, A. Forget, M. Viret, A. M. Bataille, and A. Gukasov, *Phys. Rev. Lett.* **100**, 227602 (2008).
- [17] M. Ramazanoglu, M. Laver, W. Ratcliff, S. M. Watson, W. C. Chen, A. Jackson, K. Kothapalli, S. Lee, S.-W. Cheong, and V. Kiryukhin, *Phys. Rev. Lett.* **107**, 207206 (2011).
- [18] D. Sando, A. Agbelele, D. Rahmedov, J. Liu, P. Rovillain, C. Toulouse, I. C. Infante, A. P. Pyatakov, S. Fusil, E. Jacquet, C. Carrétéro, C. Deranlot, S. Lisenkov, D. Wang, J.-M. Le Breton, M. Cazayous, A. Sacuto, J. Juraszek, A. K. Zvezdin, L. Bellaiche, B. Dkhil, A. Barthélémy, and M. Bibes, *Nature Materials* **12**, 641 (2013).
- [19] A. Agbelele, D. Sando, C. Toulouse, C. Paillard, R. D. Johnson, R. Rüffer, A. F. Popkov, C. Carrétéro, P. Rovillain, J.-M. L. Breton, B. Dkhil, M. Cazayous, Y. Gallais, M.-A. Méasson, A. Sacuto, P. Manuel, A. K. Zvezdin, A. Barthélémy, J. Juraszek, and M. Bibes, *Advanced Materials* **29**, 1602327 (2017).
- [20] A. Haykal, J. Fischer, W. Akhtar, J.-Y. Chauleau, D. Sando, A. Finco, F. Godel, Y. A. Birkhölzer, C. Carrétéro, N. Jaouen, M. Bibes, M. Viret, S. Fusil, V. Jacques, and V. Garcia, *Nat Commun* **11**, 1 (2020).
- [21] S. R. Burns, O. Paull, J. Juraszek, V. Nagarajan, and D. Sando, *Advanced Materials* **32**, 2003711 (2020).

- [22] I. Gross, W. Akhtar, V. Garcia, L. J. Martínez, S. Chouaieb, K. Garcia, C. Carrétéro, A. Barthélémy, P. Appel, P. Maletinsky, J.-V. Kim, J. Y. Chauleau, N. Jaouen, M. Viret, M. Bibes, S. Fusil, and V. Jacques, *Nature* **549**, 252 (2017).
- [23] J.-Y. Chauleau, T. Chirac, S. Fusil, V. Garcia, W. Akhtar, J. Tranchida, P. Thibaudeau, I. Gross, C. Blouzon, A. Finco, M. Bibes, B. Dkhil, D. D. Khalyavin, P. Manuel, V. Jacques, N. Jaouen, and M. Viret, *Nature Materials* **19**, 386 (2020).
- [24] I. Gross, *Exploring Non-Collinear Spin Structures in Thin Magnetic Films with Nitrogen-Vacancy Scanning Magnetometry*, *Ph.D. thesis*, Université Paris-Saclay (2017).
- [25] L. Rondin, J.-P. Tetienne, T. Hingant, J.-F. Roch, P. Maletinsky, and V. Jacques, *Rep. Prog. Phys.* **77**, 056503 (2014).
- [26] Supplemental Material giving details about the quantitative analysis of the cycloid stray field (experimental data and derivation of the analytical expression), about the wavevector ellipse and about the estimation of the topological defects size.
- [27] M. Ramazanoglu, W. Ratcliff, Y. J. Choi, S. Lee, S.-W. Cheong, and V. Kiryukhin, *Physical Review B* **83**, 174434 (2011).
- [28] X. Martí, P. Ferrer, J. Herrero-Albillos, J. Narvaez, V. Holy, N. Barrett, M. Alexe, and G. Catalan, *Physical Review Letters* **106**, 236101 (2011).
- [29] N. Domingo, J. Narvaez, M. Alexe, and G. Catalan, *Journal of Applied Physics* **113**, 187220 (2013).
- [30] D. Lebeugle, A. Mougín, M. Viret, D. Colson, and L. Ranno, *Physical Review Letters* **103**, 257601 (2009).
- [31] R. D. Johnson, P. Barone, A. Bombardi, R. J. Bean, S. Picozzi, P. G. Radaelli, Y. S. Oh, S.-W. Cheong, and L. C. Chapon, *Phys. Rev. Lett.* **110**, 217206 (2013).
- [32] N. Waterfield Price, R. D. Johnson, W. Saenrang, F. Maccherozzi, S. S. Dhesi, A. Bombardi, F. P. Chmiel, C.-B. Eom, and P. G. Radaelli, *Phys. Rev. Lett.* **117**, 177601 (2016).
- [33] B. Xu, B. Dupé, C. Xu, H. Xiang, and L. Bellaiche, *Physical Review B* **98**, 184420 (2018).
- [34] P. Schönherr, *Topological Structures in Magnetic and Electric Materials*, *Ph.D. thesis*, ETH Zurich (2018).